Exo-Earth yield of a 6m space telescope in the near-infrared

Rhonda Morgan, Dmitry Savransky, Mario Damiano, Doug Lisman, Bertrand Mennesson, et al.

Rhonda Morgan, Dmitry Savransky, Mario Damiano, Doug Lisman, Bertrand Mennesson, Eric E. Mamajek, Tyler D. Robinson, Michael Turmon, "Exo-Earth yield of a 6m space telescope in the near-infrared," Proc. SPIE 12680, Techniques and Instrumentation for Detection of Exoplanets XI, 126801L (5 October 2023); doi: 10.1117/12.2677785

SPIE.

Event: SPIE Optical Engineering + Applications, 2023, San Diego, California, United States

Exo-Earth yield of a 6 m space telescope in the near-infrared

Rhonda Morgan[a], Dmitry Savransky[b,c], Mario Damiano[a], Doug Lisman[a], Bertrand Mennesson[a], Eric E. Mamajek[a], Tyler D. Robinson[d], and Michael Turmon[a]

[a]Jet Propulsion Laboratory, California Institute of Technology, 4800 Oak Grove Dr., Pasadena, CA, 91109
[b]Sibley School of Mechanical and Aerospace Engineering, Cornell University, Ithaca, NY, 14853
[c]Carl Sagan Institute, Cornell University, Ithaca, NY, 14853
[d]Lunar and Planetary Laboratory, University of Arizona, Tucson, AZ, 85721

ABSTRACT

The Astro2020 Decadal Survey recommended a "future large IR/O/UV telescope optimized for observing habitable exoplanets and general astrophysics" that would "search for biosignatures from a robust number of about 25 habitable zone [exo]planets,"[1] now dubbed the Habitable Worlds Observatory (HWO). The search for biosignatures requires high quality spectra over a broad bandwidth and sufficient signal-to-noise. The combination of wavelength, spectral resolution, bandwidth, and signal-to-noise-ratio impacts the number of exo-Earths that can be spectrally characterized. Previous work (Morgan et al. 2022)[2] evaluated the number of Earth-size, habitable zone exoplanets (denoted here as yield) that could be spectrally characterized over the wavelength range of 500-1000 nm for a 6-m diameter exoplanet direct imaging mission for coronagraph-only and hybrid coronagraph-starshade architectures for three prior knowledge cases: the nominal case of a blind-search survey, the upper-bound case of perfect prior knowledge, which is useful to determine if target depletion occurs, and the partial prior knowledge case of a hypothetical extreme precision radial velocity survey.

In this paper, we extend previous exoplanet yields to include wavelengths out to 1.8 microns. Because the IWA for coronagraphs is proportional to wavelength, the achievable spectral coverage will be different for every planet detected. We present the spectral coverage achieved across individual target stars, as well as the ensemble target set, for a coronagraph-only architecture and a hybrid coronagraph + starshade architecture. We use the three prior knowledge cases. The coronagraph spectral characterization is simulated in the near-infrared for each of the 10% sub-bands individually, as if it were the only spectral characterization performed during the mission, and then as a broadband spectral characterization performed in sequence over the sub-bands. The starshade achieves the broadband spectral equivalent simultaneously. We also examine the capabilities of the 60 m starshade point design and investigate the benefits of refueling.

Keywords: exoplanets, coronagraph, starshade, LUVOIR, HabEx, extreme precision radial velocity, HWO, Future Great Observatory

1. INTRODUCTION

The Astro2020 Decadal Survey recommended a "future large IR/O/UV telescope optimized for observing habitable exoplanets and general astrophysics" to be mature in concept by end of the decade and to be launched in the early 2040's. Astro2020 puts forward a mission "capable of surveying a hundred or more nearby Sun-like stars to discover their planetary systems and determine their orbits and basic properties" and recommended as the exoplanet science goal "to search for biosignatures from a robust number of ∼25 habitable zone [exo]planets." The Decadal Survey recommended a mission maturation program to "optimize configurations targeted at performance consistent with the target 6-m off-axis aperture as indicated in Figure

Send correspondence to R.M.: rhonda.morgan@jpl.nasa.gov

Techniques and Instrumentation for Detection of Exoplanets XI, edited by Garreth J. Ruane, Proc. of SPIE Vol. 12680, 126801L · © 2023 SPIE
0277-786X · doi: 10.1117/12.2677785

7.6." Figure 7.6 of the Decadal Survey shows that for a 6-m off-axis aperture, 25 is the "potentially habitable exoplanet yield."

It is worth pausing to understand the nuance of what is meant by yield in Figure 7.6 of the Decadal Survey. The yield calculation for Figure 7.6[3] was performed using a water-search yield metric. This metric is defined as the number of exo-Earth candidates that are spectrally characterized from 800–1000 nm at signal-to-noise ratio (SNR) of 5, and spectral resolution of 70.[4] Spectral retrieval simulations indicate that a spectral resolution of 70 and an SNR of 5 is the minimum needed to detect that water line at 940 nm.[5] Also, a methane line at 890 nm could be strongly present in the Archean Earth and in gas giant atmospheres. The water search metric is a useful metric for coronagraphs which offers the smallest investment of integration time to determine if the exoplanet is compelling and worth further spectral observation.

Further spectral lines of interest including oxygen at 760 nm in the visible, ozone at 320 nm in the near ultraviolet (NUV), and in the near infrared (NIR) carbon dioxide at 1.59 μm and methane at 1.69 μm. The quality of spectra needed for spectral retrieval to identify these molecular species was established by the HabEx and LUVOIR Concept studies[6,7] and has been an ongoing topic of discussion and active research.[8,9] We adopt the spectral qualities used by the HabEx and LUVOIR studies and by the Exoplanet Exploration Program Office's Yield Standards Evaluation Team[10] for broadband spectra metrics in the visible and in the NIR.

The metric is a description of the quality of the spectra obtained during spectral observations and is described by the spectral resolution, SNR, wavelength, and bandwidth (BW). These four properties of the spectral observation impact the exposure time and thus the yield.

The wavelength also impacts the yield for coronagraphs via the inner working angle (IWA), which describes the closest separation between planet and star that can be observed by the instrument. The IWA for a coronagraph is proportional to the wavelength divided by the diameter of the aperture, so that bluer wavelengths will have a smaller IWA for the same aperture. The IWA for a starshade is driven by the geometry of the starshade relative to the telescope and is proportional to the diameter of the starshade divided by the starshade-telescope separation. The IWA is the same for all wavelengths in the starshade bandpass at this particular separation. The starshade-telescope separation can be changed to shift the wavelength range of the starshade, which results in a new IWA.

We the yield of broadband spectral characterizations in the visible and NIR wavelengths and compare them to yields for the water search metric. In the Sec. 2 we describe the broadband spectral characterization metrics (Sec. 2.1), then we describe the coronagraph-only and the coronagraph+starshade architectures and their observing scenarios in Sec. 2.2. In Sec. 2.3 we describe the three prior knowledge cases and how they alter the observing scenarios. We present yield results for the visible wavelengths in Sec. 2.4. We describe the NIR metrics and observing scenarios in Sec. 3 and present NIR yields results in Sec. 3.3. We explore the retargeting slew capacity of the starshade in Sec.4 and show an preliminary study on the benefits of refueling the starshade in Sec. 4.1. We provide an overview of the modeling tool and approach in Sec. 5 and conclude with some thoughts on broadband spectral characterization in Sec.ẽfsec:conclusion.

2. VISIBLE WAVELENGTH SPECTRAL CHARACTERIZATION

We evaluated two architectures (coronagraph-only and hybrid starshade + coronagraph) using the broadband metric. For this assessment of yield for a 6-m off-axis space observatory, we scaled HabEx up to 6 m. We used the same starlight suppression performance as the HabEx vector vortex coronagraph in λ/D but used 6 m for the diameter. We used the HabEx optical throughput for the non-coronagraph optics which includes polarization splitting. We used the new starshade point design for HWO by Shaklan et al 2023,[11] which is 60 m in diameter with a 65 mas inner working angle (IWA) at the tips. The starshade dry mass was scaled from the HabEx (52 m diameter) and Roman Space Telescope Rendezvous Concept (26 m diameter) designs. The list of instrument parameters is given in Section A.2.

2.1 Broadband Metrics

The broad-spectrum metric covers 500 nm to 1000 nm. We use a high quality spectra (R=140, SNR=10) for the region from 700–1000 nm where multiple biomarker species of interest could be detected. The quality is sufficient to detect oxygen at 760 nm for a Modern Earth twin. Then from 450–700 nm the quality of spectra is reduced to save integration time, because the goal of this wavelength region is the detection of Raleigh scattering, not detection of specific molecular species. The broadband spectra are observed serially through four sub-bands of 20% BW for a coronagraph. We provided some overlap of the sub-bands to allow for band-to-band stitching. We imposed the mission integration time limit to the total integration time of the four bands.

The starshade covers the spectral range of 500 nm – 1000 nm in a single passband. The spectral resolution at a desired wavelength will be achieved over the entire broad spectrum. The broadband visible starshade and coronagraph metrics, as well as the water search metric, are shown in the bottom row of Figure 1 for a synthetic spectra with added noise for an Earth-Sun twin at 7.5 pc.

2.2 Architectures

The hybrid architecture (C+S) uses both a coronagraph and a starshade. The coronagraph is used for the photometric blind search and photometric imaging for astrometric measurements that are used to determine the exoplanet's orbit. The starshade is used for spectral characterization. This architecture combines the complementary strengths of the coronagraph (agility) with the strengths of the starshade (broadband spectra with high throughput and a wide OWA). In the hybrid architecture observing scenario, the blind search survey images stars, then repeats the imaging observation at an epoch one-third of an Earth equivalent insolation distance (EEID) orbital period later. After two null detections, the target is dropped from observation. After a successful detection, the target is revisited every one-third of an EEID period until four detections succeeded that span more than half the period of the planet. Its orbit thereby known,[6,10,12] the target is then promoted to the pool of targets for spectral characterization. The spectral characterization targets are scheduled for observation by the starshade using a two-step look ahead Traveling Salesman Problem (TSP) optimizer. The spectral characterization targets have top priority versus other targets farther back in the funnel. While the starshade is transiting to a new target, the telescope continues with the blind search and orbit determination or performs general astrophysics observations.

In the Coronagraph-only architecture (C), the blind search is conducted as with the coronagraph in the hybrid architecture. Once a target is promoted for spectral characterization, the targets are observed spectrally as soon as a sufficiently long observing window is available and in order of completeness divided by integration time. The spectral characterization observations always have priority over photometric imaging observations.

2.3 Prior Knowledge Cases

The no-prior-knowledge case is the blind search case described above for for the architectures in Section 2.2. It is the baseline case in the HabEx and LUVOIR concept studies.

The perfect prior case skips the blind search and orbit determination and performs only spectral characterization. It adheres to realistic mission constraints like solar avoidance, planet propagation, and observation scheduling. The perfect prior case uses the exoplanet properties, such as orbit, radius, and albedo, which are assumed to be known, to observe when the exoplanet is at maximum elongation and to determine the optimal exposure time. The perfect prior case provides an upper bound to the spectral characterization yield that adheres to mission constraints, such as solar avoidance, observatory orbit, and observation scheduling.

Yields between the lower bound of the blind search case and the upper bound of the perfect prior case may be achieved with partial knowledge. We evaluated one particular case of partial knowledge, which is a hypothetical future Extreme Precision Radial Velocity (EPRV) instrument with 3 cm/s precision, which could detect Earth-size exoplanets in habitable zones. To implement the EPRV prior knowledge case, we used an EPRV sensitivity heuristic that would determine whether or not a synthetic exoplanet would be detectable by EPRV. Details of the EPRV sensitivity heuristic and the per-star probability of EPRV detection can be

found in Refs. 13, 14. Any synthetic planets that could be detectable by EPRV were considered positive EPRV detections and were promoted for spectral characterization. This has a huge impact on yield at the start of the mission, which reduces risk and gives more mission time to respond to discoveries, to plan, and to perform follow-up observations on intriguing candidates. The null detections of EPRV were not used, though doing so would likely increase observing efficiency and thereby increasing yield.

2.4 Visible Wavelength Yields

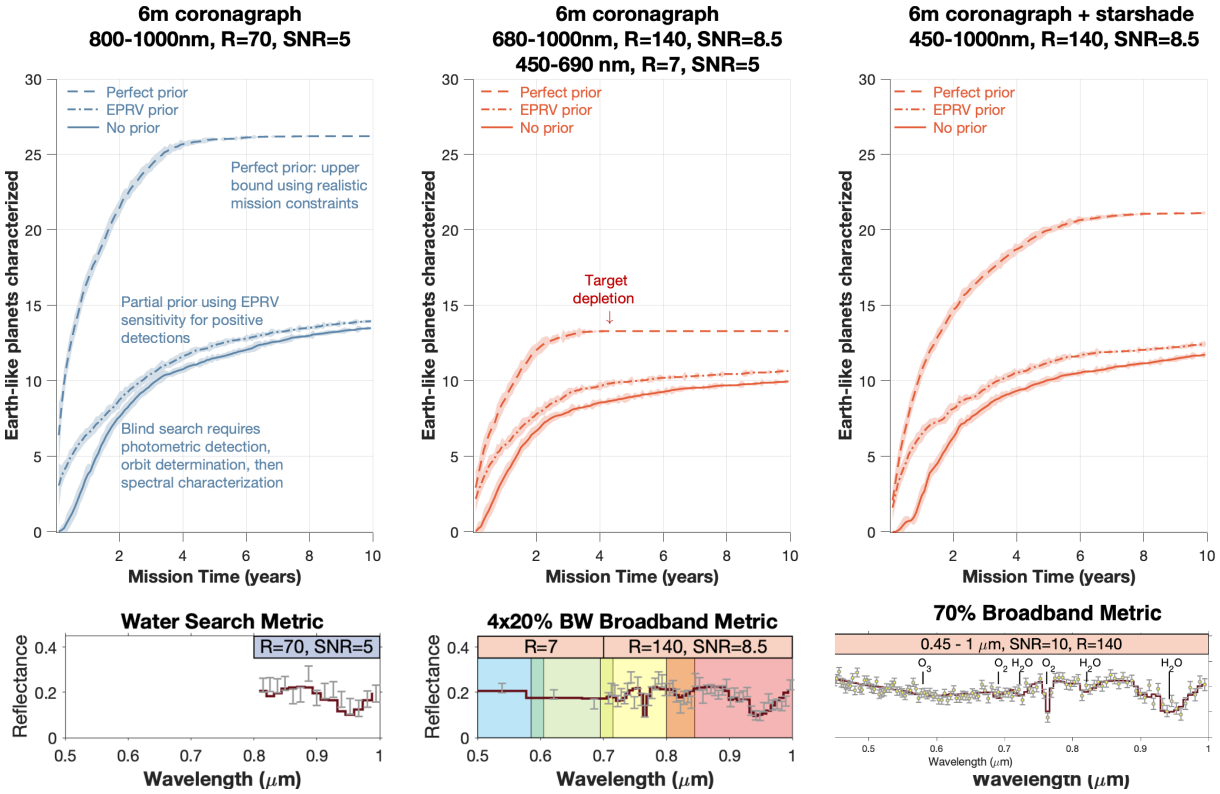

Figure 1. The yield as a function of mission time is shown for a 6-m off-axis coronagraph space telescope. The top left plot shows yield with the water search metric which uses a single coronagraph 20% sub-band. The top middle plot shows yield for a broadband spectra comprised of four, sequentially acquired, 20% sub-bands in which the bluest two have reduced spectral resolution which saves integration time while remaining sufficient for detecting Rayleigh scattering. The top right plot shows the equivalent broadband spectra for a starshade. The three prior knowledge cases (no prior, partial prior and perfect prior) are given by the solid, dot-dash, and dashed lines, respectively. The bottom row shows the corresponding synthetic spectra with added noise for an Earth-Sun twin at 7.5 pc. The magenta line is the Earth's spectrum at the goal spectral resolution.

The yield is shown over mission elapsed time because our modeling tool (see Sec. 5) schedules observations and responds dynamically during the simulation to the discovery of exoplanets and other observational results. The simulations are structured such that each specific metric is the only spectral characterization that is performed on each candidate exoplanet. This allows us to examine the bounding yield for each metric individually. A future exoplanet direct imaging mission would likely perform a variety of spectral characterizations and use a combination of these and other metrics. The HabEx and LUVOIR studies used a five-year mission with 50% of the time allocated to exoplanet observations. In thise study, we extend the simulated mission time to ten years to investigate the timeline for target depletion. The use of observing time for exoplanets is enforced via a sliding window average of 50%. The results are shown for three cases of prior knowledge: no prior knowledge, partial prior knowledge, and perfect prior knowledge.

2.4.1 Water Search Metric Yields

The leftmost plot of Figure 1 shows the yield as a function of mission elapsed time for the three prior-knowledge cases. The perfect-prior knowledge case climbs steeply as the nearby, easy targets are spectrally characterized and then the slope diminishes as the longer integration time targets are characterized. When the line flattens to horizontal, target depletion is reached. This occurs at about when five years of mission time is elapsed. The perfect prior yield for the water search metric is 26 Earth-size exoplanets.

The no-prior knowledge, or blind search, case begins slowly while the blind search survey and orbit determination are carried out. Then the slope becomes steep which indicates characterization of the shorter integration time targets. As longer integration times are required for both spectral characterization and the ongoing blind search survey, the yield slope decreases. The yield continues to slowly increase at ten years of mission elapsed time. The no-prior yield for the water search metric is 13.5 Earth-size exoplanets.

The EPRV partial prior knowledge case begins with immediate characterization of EPRV-detectable targets (that meet mission constraints). This accelerates the timeline for achieving yield. In this example, half of the EPRV yield is achieved in 450 days while the blind search achieves half of its yield in 642 days. Achieving yield earlier in the mission provides exciting results sooner to the science community and the public and provides a longer runway of remaining mission to respond to discoveries which could update the observing approach. Achieving yield sooner is also helpful for mission risk mitigation. The EPRV-prior yield for the water search metric is 14 Earth-size exoplanets.

2.4.2 Broad Spectrum Metric Yields

For the coronagraph-only architecture, the broadband spectrum is observed serially through four sub-bands of 20% BW. The middle plot of Figure 1 shows the yield results. The perfect prior yield is 13.3 exo-Earths and reaches target depletion at four years of mission elapsed time. The no-prior blind search survey case has a yield of 10 exo-Earths. A yield of 8 exo-Earths at 5 years of mission elapsed time; an additional five years of mission time is required to achieve two additional exo-Earth broadband characterizations. The EPRV prior case achieves half of its yield of 10.6 exo-Earths at 275 days of elapsed mission time, which is less than a year into the mission. This is a significant improvement over the 500 days needed by the no-prior blind search case to achieve half of its yield.

For starshade spectral characterization, a broad band of 67% BW is observed simultaneously from 500 nm - 1000 nm at the spectral resolution of 140 and SNR of 8.5. The rightmost plot of Figure 1 shows the yield for the hybrid coronagraph + starshade architecture in which the spectral characterization is performed by the starshade and the photometric detections for blind search and orbit determination are performed by the coronagraph. The perfect prior knowledge case shows the capacity of the starshade to perform spectral characterization while abiding by solar constraints and starshade retargeting slews. The perfect prior yield is 21.1 exo-Earths, much higher than the coronagraph-only perfect prior yield of 13.3 due to the throughput and IWA advantage of the starshade. The EPRV prior knowledge case also leverages the throughput advantage of starshades to achieve half of this cases's yield at 335 days, less than a year into the mission, and full yield of 12.5 exo-Earths at ten years of mission elapsed time. The no-prior blind search survey case achieves half of its yield 670 days into the mission and full yield of 11.5 exo-Earths at ten years of mission elapsed time.

The starshade, with its throughput and IWA advantage, achieved 50% higher yield for the perfect case than the coronagraph, almost 20% higher yield for the EPRV prior case, and 17% higher yield for the no-prior blind search case. Additionally, EPRV prior knowledge accelerated mission yields such that half of the end-of-mission yields were achieved within the first year of the mission for both the coronagraph and the starshade.

3. NEAR INFRARED SPECTRAL CHARACTERIZATION

3.1 Coronagraph - only

The near-infrared (NIR) wavelength range from 1 – 1.8 μm utilizes a different detector and optical channel from the visible coronagraph. In the LUVOIR Final Report,[7] the infrared coronagraph is placed at the end

of a series of dichroic filters for the near-ultraviolet and visible coronagraphs. The spectral characterization occurs in 10% bandwidth sub-bands with spectral resolution of 40 and an SNR of 8.5. We calculate the upper bound of achievable yield in a sub-band by simulating an observing scenario in which spectral characterization is performed only in that sub-band. The water spectral search is not performed first, the visible broadband spectra is not performed; only the NIR sub-band is spectrally characterized. We then calculate the yield for spectral characterization of the NIR sub-bands in sequence to accumulate a broad-band spectra. For this scenario, we impose a 60 day integration time limit on the cumulative integration time of all the sub-bands. The blind-search survey is performed in the blue end of the visible coronagraph, the same as when visible characterization is performed.

3.2 Coronagraph + Starshade

The coronagraph performs the blind-search survey in the visible and the starshade performs the spectral characterization in the NIR. We use the 60 m point-design starshade by Shaklan et al. 2023 and change the separation distance from 95,200 km to 52,900 km so that the red-edge wavelength of the passband had been 1000 nm becomes 1800 nm. The blue-edge of the 67% passband becomes 900 nm. The broadband spectra from 900 – 1800 nm is achieved in a single observation. We use a spectral resolution of 40 and an SNR of 8.5, as with the coronagraph NIR spectra.

3.3 NIR Results

When all of the spectral characterization time is dedicated to the 1000 – 1100 nm sub-band, the perfect prior yield is about 12.5 exo-Earths and for the baseline blind-search is about 9 exo-Earths as shown in Figure 2. The yield decreases as the sub-band moves to the right largely due to geometry as the inner working-angle of the coronagraph is proportional to wavelength; as the wavelength increases, the inner working angle also increases and fewer habitable zones remain accessible. This can be seen in Figure 3 comparing the per-star yields at the bluest and reddest sub-bands of the NIR coronagraph.

At the reddest sub-band of 1600 – 1800 nm, the perfect prior yield is about 6 exo-Earths and the blind-search survey yield is about 4 exo-Earths. This is very close to the yields for broadband NIR spectra that is acquired sequentially through all of the sub-bands. The broadband spectra are limited by the geometric accessibility of habitable zones at the longest wavelength. The additional integration time for the other sub-bands does not alter the yield significantly.

Broadband spectra can also be achieved using a starshade that covers the entire 900 – 1800 nm passband (67% bandwidth). The spectra is observed simultaneously over the entire passband. For the perfect prior case, the starshade yield is 6.5 exo-Earths, almost 10% higher that the coronagraph broadband perfect prior case. For the baseline blind search case over the broadband, the yield is the same for the coronagraph and starshade, once again suggesting geometry to be the main limitation at the longest wavelength.

4. STARSHADE CAPABILITY

The starshade for the HabEx concept study, working in complimentary fashion with a coronagraph, executed an average of 115 retargeting slews over a five year mission. We examined if the Shaklan et al. point design for a 6m space telescope would have as much capacity, and we extended the simulated mission time to ten years to more readily when target depletion occurs. HabEx combined three starshade surveys to arrive at 115 retargeting slews. For simplicity, we consider the single survey for broadband visible spectra discussed in Section 2. We utilize the perfect prior case, because it has the largest number of retargeting slews, and we increase the number of visits to each target to three. Doing this achieves over 50 retargeting slews, and uses just over 20% of the mission time on observing spectra. The starshade has copious idle time, so we simulated a rendezvous mission variation in which the starshade had a delayed launch and joined the observatory two years into the mission. Even in this rendezvous scenario, the starshade has sufficient time for 50 retargeting slews and plenty of idle time and achieves the same yield as beginning characterization at the start of the mission. The capability of this starshade point design was not challenged by this observing scenario.

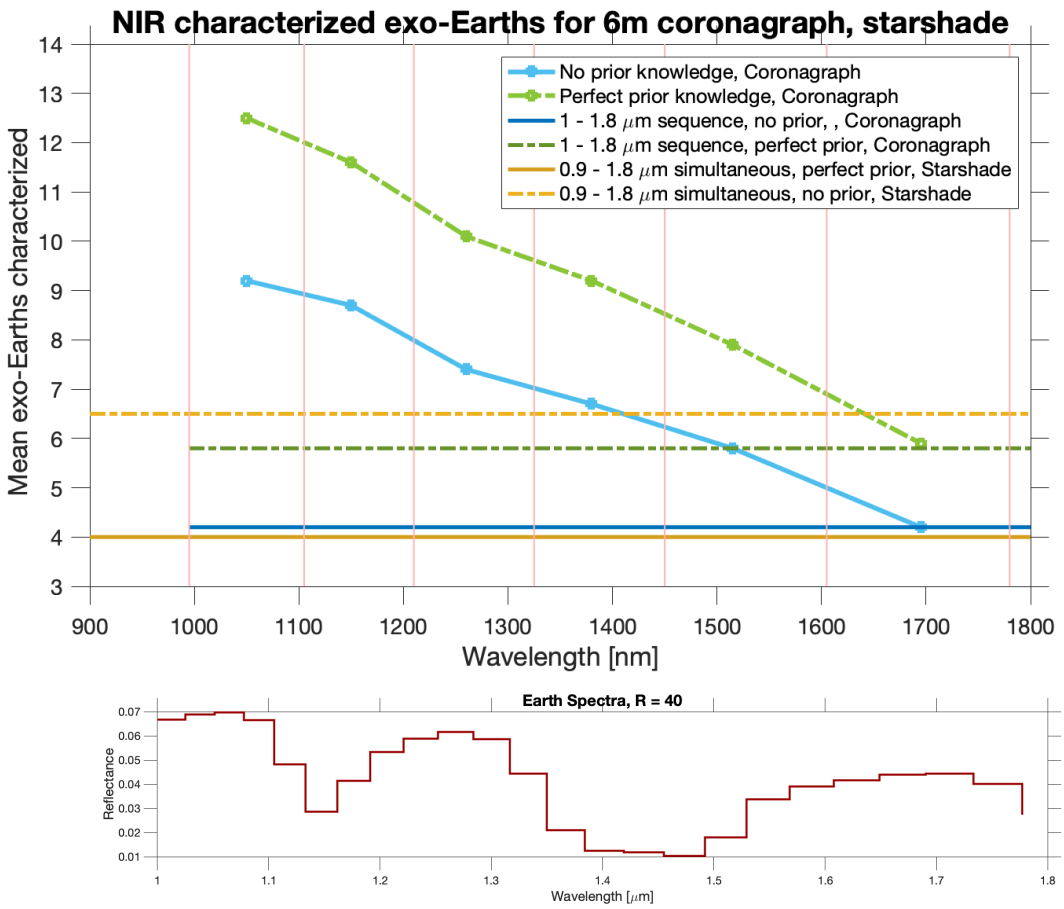

Figure 2. The NIR spectral characterization yield for a ten-year mission is shown for a 6-m off-axis space telescope performing spectral characterization with a coronagraph or starshade. The yield for each coronagraph sub-band is the upper bound when all characterization integration was spent on that sub-band. The green and blue horizontal lines indicate yield for a broad-band spectra built-up sequentially over all coronagraph sub-bands. The horizontal yellow lines show the starshade yield which is acquired simultaneously over its 67% bandwidth passband. The red vertical lines indicate the sub-band edges. The corresponding spectral quality at R=40 is shown in the bottom row. The two prior knowledge cases (no prior and perfect prior) are given by the solid and dashed lines, respectively.

4.1 Refueling

We also conducted a preliminary study on the impact of refueling the starshade. We used the perfect-prior case with three characterizations per target to have a large number of retargeting slews. Then we simulated the ability to refuel the starshade fuel tank whenever the fuel became too low to complete the next retargeting slew. We automatically refueled the starshade assuming a capacity for 1000 kg of fuel on board. The same yield was achieved with refueling, which is expected for the perfect-prior case. Significant improvement was seen with slew duration and total fuel consumed.

The average slew duration decreased from 16.9 days to 12.6 days. The histogram in Figure 5 of slew duration shows that refueling eliminated slews longer than 20 days. Shorter slews allow for a more agile starshade and should produce greater efficiency of starshade spectral observations for scenarios that are target-rich.

The total fuel consumed was reduced from 9500 kg to 6800 kg, a savings of 40%. The dry mass of the starshade was 5600 kg. Without refueling, the fuel consumed was almost twice the dry mass of the starshade. With refueling, the on-board fuel mass never exceeded 15% the total mass of the space vehicle. In the simulation, the fuel is the total of the solar electric propulsion fuel for retargeting transits and the

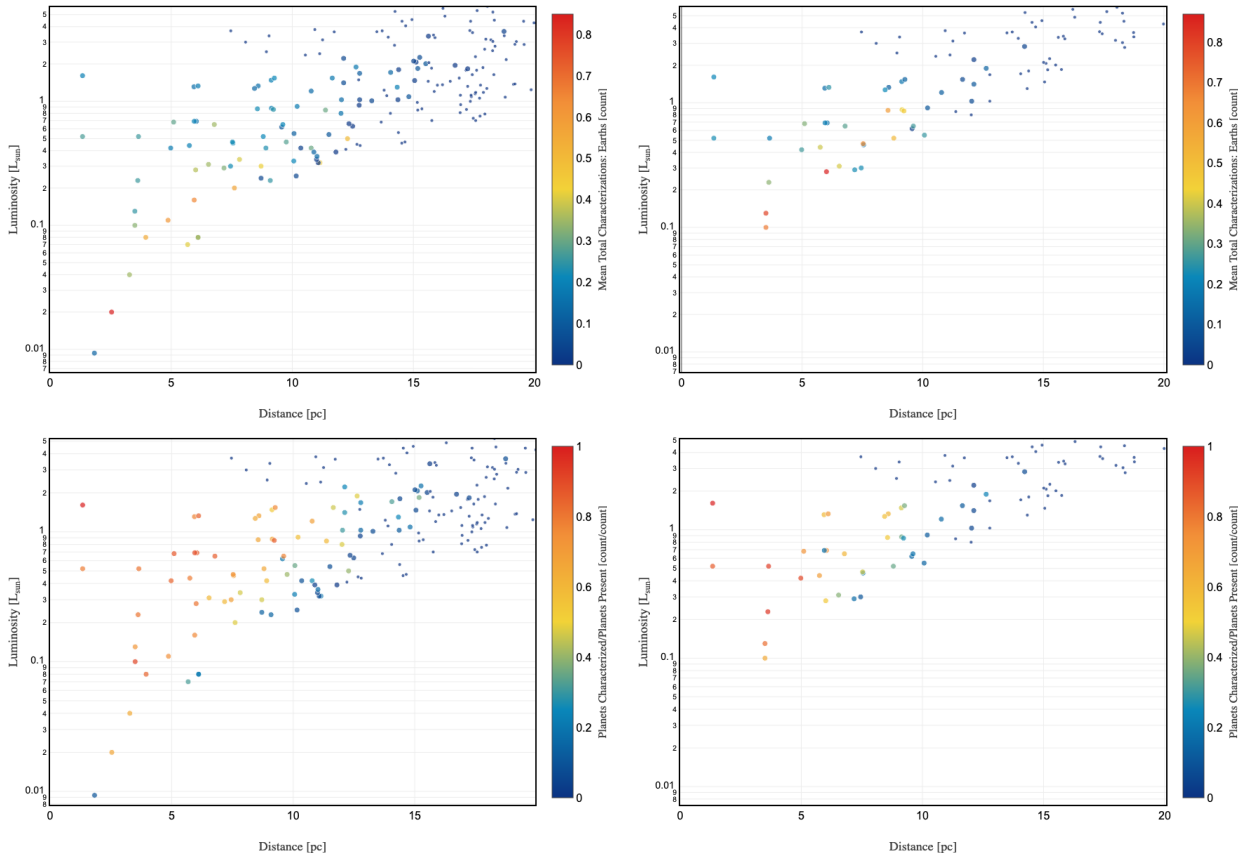

Figure 3. The per star yield for a 6m coronagraph-only architecture is shown where the stars are plotted by distance versus luminosity. The top row shows the mean total characterized exo-Earths per star. The bottom row shows the fraction of exo-Earths characterized to exo-Earths present. The left column is the 1000-1100 nm sub-band and the right column is the 1600-1700 nm sub-band. The smaller blue markers are stars on the target list that were not observed in the simulated mission. The lower right, curving edge of the star population is due to IWA limitations.

liquid propellant used for formation maintenance while observing. Allowing the total fuel to be replenished saved fuel both for retargeting slews and formation maintenance. The savings in fuel and the shortened duration of slews is due to having a smaller total mass to move via the rocket equation.

5. OVERVIEW OF YIELD CODE

We used EXOSIMS[15] to perform all of the yield modeling in this study. EXOSIMS is an open-source, parametric, Python-language exoplanet direct imaging mission simulation code. As illustrated in Figure 6, EXOSIMS includes an astrophysics simulation of synthetic exoplanets and astrophysical noise sources; an instrument performance model to calculate signal, noise, and integration time; and a mission model to simulate the orbital dynamics of the observatory's orbit and the solar system bodies for stray light avoidance. EXOSIMS creates Monte Carlo ensembles of end-to-end missions with observation scheduling. Here we provide an overview of EXOSIMS. More detailed description can be found in Refs. 10, 13.

EXOSIMS is a Monte Carlo Mission Scheduling (MCMS) simulation code that simulates Monte Carlo universes. For a single universe simulation, synthetic planets are drawn from planet property distributions, and then an end-to-end mission is simulated. The mission is dynamically, sequentially scheduled and executed: the next targets to be scheduled respond to the results of previous observations (successful, null, or false positive). EXOSIMS consists of a collection of modules, abstracting out various state variables and methods associated with different aspects of the full mission simulation, all with a strictly defined in-

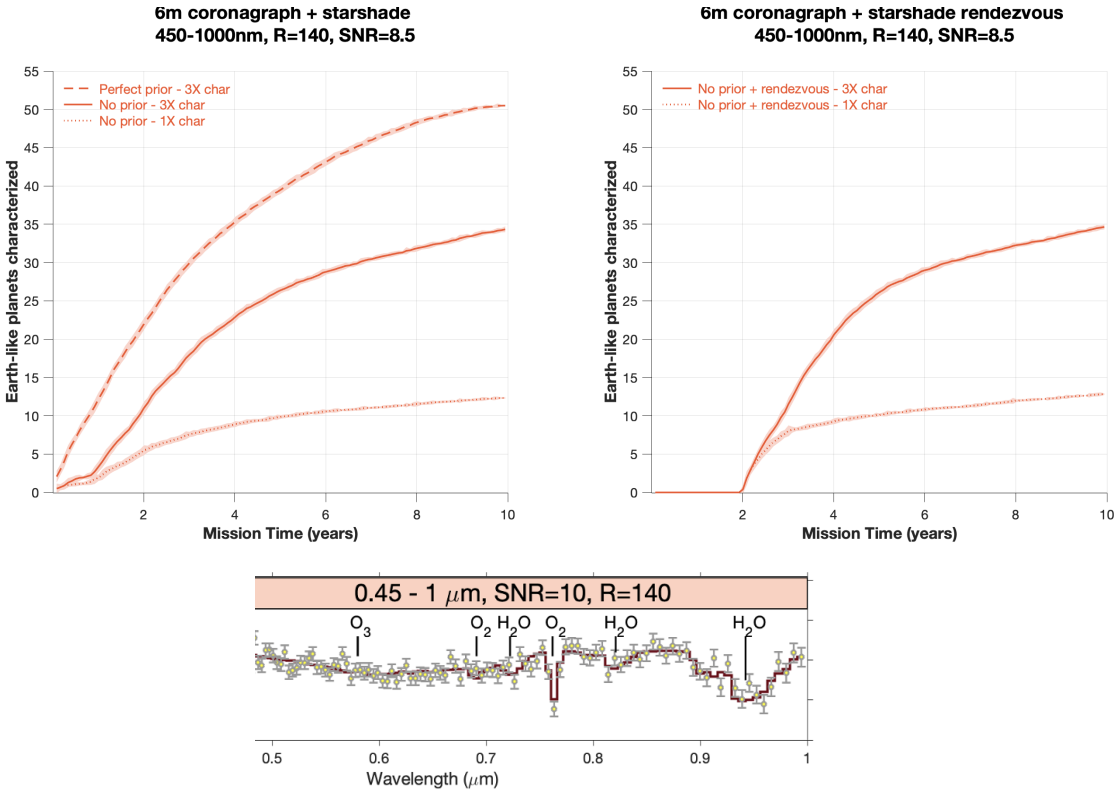

Figure 4. The left plot shows the perfect prior (dashed line) with three characterizations per target: the baseline no-prior knowledge case with three characterizations per target is shown as a solid line and the single characterization per-target yield is shown as a dash-dot line. The right plot shows the yield with a delay start to the spectral characterization for three characterizations per target (solid line) and a single characterization per target (dash-dot line) for the baseline no-prior case. The two-year delay start achieves the same yield as on the left.

put/output specification. This allows for modules to be extended, or for new modules to be implemented, without requiring any modifications to other portions of the code. EXOSIMS is thus adaptable to entirely new designs for instruments, observatories, or overall mission concepts. Figure 7 shows a schematic representation of how an EXOSIMS Mission Simulation object is constructed out of the individual modules. The module functionality split is further described in Ref. 13.

Yield is calculated from a generated Survey Ensemble, which contains the outputs of N Survey Simulations, each of which uses exact copies of all of the downstream modules, except for the Simulated Universe. The Simulated Universe is re-generated for each individual mission simulation by re-sampling the planet population distributions and synthesizing a new set of planets. The execution of a single mission simulation occurs within a top-level loop which selects each subsequent target from the pool of 'currently' (at the current simulated mission time) available targets, calculates the required integration time, simulates the observation and then simulates the outcome, which can be a true positive (detection), false positive (misidentified speckle or background object), true negative (null detection) or false negative (missed detection).

The Survey Simulation scheduler module is the backbone of EXOSIMS. It drives the dynamic observing sequence and contains the logic for autonomous target selection. Multiple Schedulers exist for EXOSIMS, each tailored to an architecture and an observing scenario. The Weighted Linear Cost Function (WLCF) scheduler is used for architectures having a starshade (6m C+S). For coronagraph-only architectures, a simplified WLCF scheduler is used.

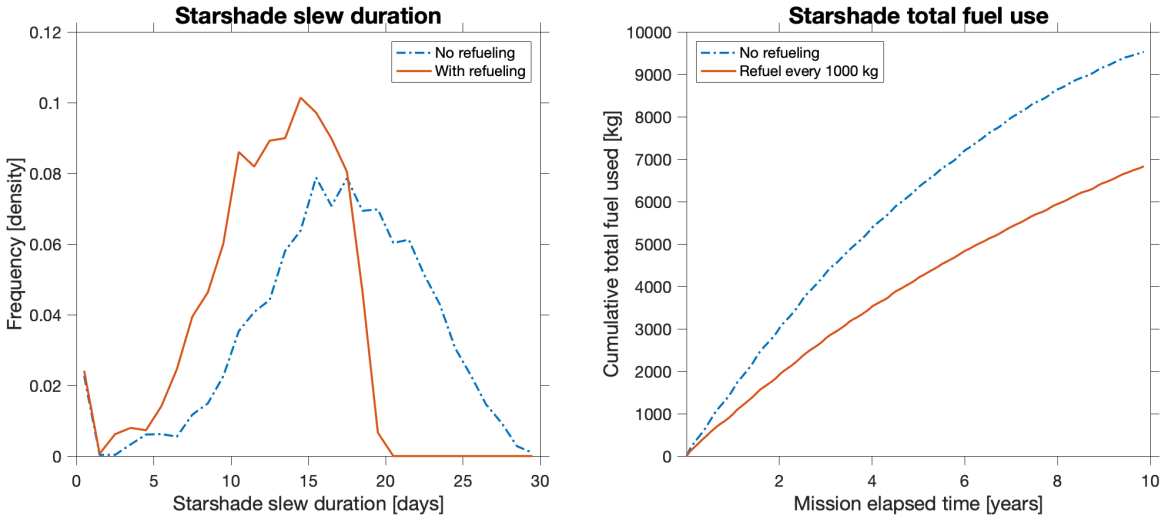

Figure 5. In the most taxing observing scenario, refueling every 1000 kg shortens the average retargeting slew duration from 16.9 days to 12.6 days (left) and reduces the total fuel consumed from 9500 kg to 6800 kg (right).

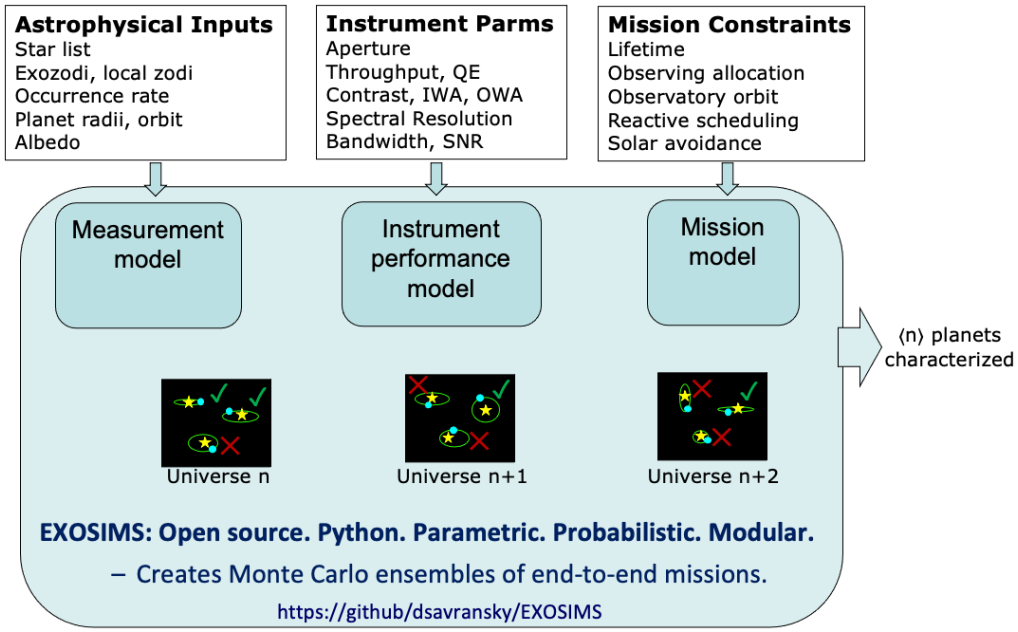

Figure 6. EXOSIMS is an open-source, parametric, python-based exoplanet direct-imaging mission simulation code. EXOSIMS creates Monte Carlo ensembles of end-to-end missions with observation scheduling.

6. CONCLUSION

We evaluated the potential exoplanet science return for the Decadal-recommended Habitable Worlds Observatory. As a notional design for a 6-m off-axis, exoplanet direct imaging observatory, we scaled the HabEx concept design up to 6m. We assessed two architectures: a coronagraph-only architecture and a coronagraph + starshade architecture. For the coronagraph we used the HabEx vector vortex charge 6 design and for the starshade we used a 60-m diameter point design for HWO by Shaklan et al.[11] We assessed the science return for Earth-size habitable zone exoplanets in the visible spectrum using three different metrics to express the quality of the spectra: a water search metric (R=70, SNR=5, BW=20%), a broadband spectrum metric for coronagraph the uses four 20% sub-bands in series (500–700 nm: R=7, SNR=8.5, 700–1000 nm:

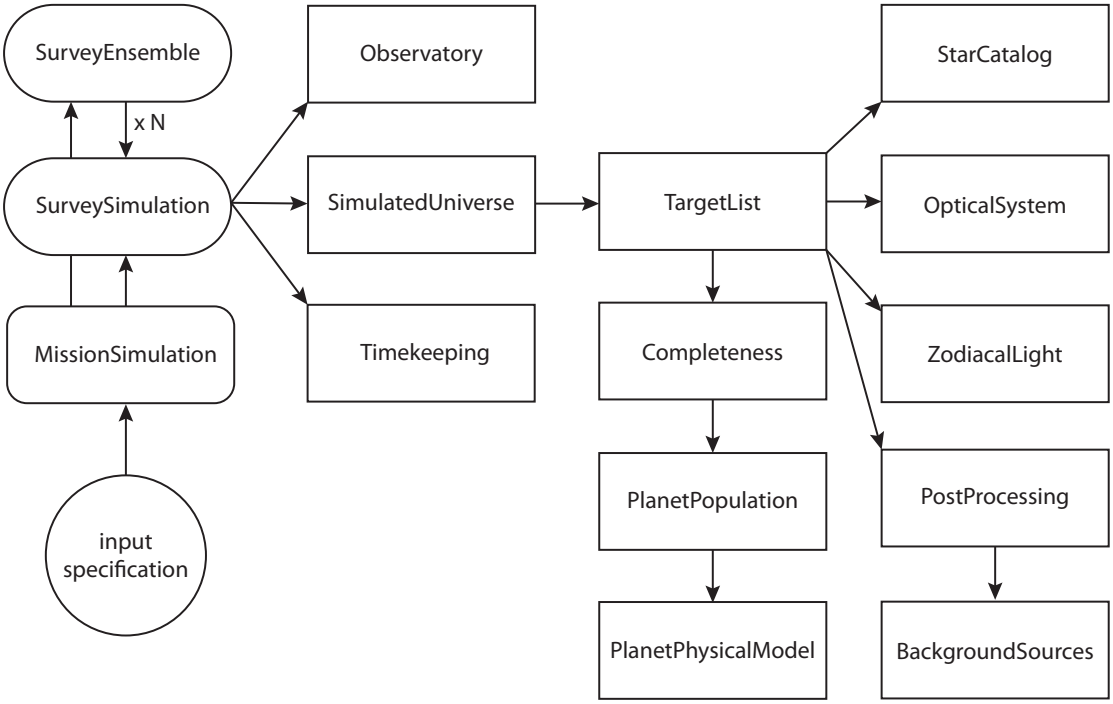

Figure 7. Schematic depiction of the instantiation path of all EXOSIMS modules. The arrows represent instantiation of an object, and object references to each module are always passed up directly to the top calling module, so that a given module has access to any other module connected to it by a direct path of instantiations. For example, TargetList has access to both PostProcessing and BackgroundSources, while Observatory does not have access to any other modules. The typical entry point to EXOSIMS is the construction of a MissionSimulation object, which causes instantiation of SurveySimulation, which in turn instantiates all the other modules.

R=140, SNR=8.5), and a broadband spectrum metric for a starshade that covers 500–1000 nm at R=140, SNR=8.5. We evaluated the yield results using three levels of prior knowledge: no prior knowledge, partial prior knowledge, and perfect prior knowledge.

The perfect prior knowledge case provides an upper bound on spectral characterization by skipping the blind-search and performing only spectral characterizations while abiding by realistic mission constraints such as solar avoidance, starshade retargeting slews, and observation scheduling. The perfect prior knowledge case yield for the water search metric was 26, for the coronagraph visible broadband metric was 13, and for the starshade visible broadband metric was 21. The starshade 67% bandwidth yield was 80% of the coronagraph yield for the water search metric. The perfect prior results show that spectral characterization is not limited by the retargeting times of the starshade.

For the no-prior-knowledge blind-search case, the coronagraph performs the blind-search survey with photometric detections, then performs spectral characterization with either the coronagraph or the starshade. When sharing the mission time between the blind search and spectral characterization, the integration time plays an important role; this can be seen in the coronagraph going from the water search metric with a yield of 13.5 to a yield of 10 for the broadband metric, which has four sub-bands, two of which use twice the spectral resolution and almost twice the SNR. The starshade yield is nearly 12 exo-earths. This results highlights the complimentary strengths of a starshade paired with a coronagraph.

The EPRV partial prior knowledge case accelerated results by achieving half of its broadband characterization yield in the first year of the mission for both the coronagraph and the starshade. For the water search metric, EPRV prior knowledge achieved half of the yield results in the first 14 months of the mission. Accelerated spectral characterizations allow for more opportunities of follow-up observations of compelling targets during the mission lifetime as well as mission risk mitigation.

The NIR broadband spectra for the coronagraph was composed of six 10% BW sub-bands at R=40, SNR=8.5. The yield was evaluated for the broadband spectra as well as each sub-band individually. The yield of each sub-band decreased with increasing wavelength due to the wavelength dependence of the coronagraph IWA. The no-prior-knowledge case for the coronagraph achieved 9 exo-Earths for 1000–1100 nm and just under 6 exo-Earths for 1600–1800 nm. The broadband yield was just under 6 exo-Earths, the same as for the 1600—1800 nm sub-band. This suggests that geometry drives the access the habitable zones in the NIR.

The starshade covers the entire 900-1800 nm passband in a single observation. For the perfect prior case, the starshade yield is 6.5 exo-Earths, almost 10% higher that the coronagraph broadband perfect prior case. For the no prior knowledge blind search case, the yield is the same for the coronagraph and starshade, once again suggesting geometry to be the main limitation at the longest wavelength.

We investigated the retargeting capabilities of the starshade. We attempted to create an observing scenario with a large number of retargeting slews by using the perfect-prior-knowledge case for visible-wavelength broadband characterization and three observations per target. This scenario did not challenge the retargeting capacity of the starshade. We simulated a two-year delay in the start of the starshade portion of the mission and still did not tax the retargeting capacity of the starshade.

We performed a preliminary study of refueling the starshade. We simulated automatic refueling of the starshade every 1000 kg of fuel consumption. The total fuel consumed was reduced from 9600 kg to 6800 kg, a savings of 40%. The average retargeting slew duration decreased from 16.9 days to 12.6 days and the maximum slew duration shortened from 30 days to 20 days. The benefit is due to moving around less mass with starshade via the rocket equation.

In summary, we have evaluated broadband spectral characterization yields for Earth-size planets in the habitable zone of nearby stars and found that both coronagraphs and starshades are capable of providing broadband spectrum in the visible and NIR wavelengths. Starshades offer the advantage of broadband spectra observed simultaneously while coronagraphs observe sequentially through 10% or 20% BW sub-bands. Starshades also offer a throughput advantage that allows for higher yields in the visible, and only slightly higher broadband yields in the NIR due to geometry-driven limitations.

APPENDIX A. YIELD MODELING

A.1 Astrophysical Inputs

The astrophysical assumptions and inputs are summarized here and discussed in greater detail in the ExSDET Final Report of the Common Comparison of HabEx and LUVOIR.[10] The astrophysics input parameters are summarized in Table 1.

The exoplanet occurrence rates were based on the EXOPAG SAG-13 power law model of Kepler data, as modified by Dulz et al.[16] for large mass and large semi-major axis planets.

Exo-Earth candidates were assumed to be on circular orbits and to reside within the conservative HZ, spanning 0.95 – 1.67 AU for a solar twin.[17] Exo-Earth candidates span radii ranging from $0.8a^{-0.5}$ to 1.4 $R_\oplus$, where a is the semi-major axis. This study focused on the exo-Earth candidate populations, using joint radius and semi-major axis distributions.

The stray light from binary stars in the final image plane was estimated[18] and included as an astrophysical noise source in exposure time calculations. AYO and EXOSIMS made no artificial cuts to the target list based on binarity. Instead, each code determined whether or not stray light noise made a target unobservable.

Zodiacal cloud brightness was estimated as a function of wavelength and ecliptic latitude and longitude by interpolating published tables.[19] EXOSIMS specifically schedules each observation, enabling it to compute the zodiacal brightness based on the target's ecliptic coordinates on the date of the observation.

The exozodiacal light level used in the yield simulations were taken from the recent results of the Large Binocular Telescope Interferometer (LBTI) survey of exozodiacal dust.[20] The nominal distribution function of the luminosity was used to draw an exozodiacal brightness for each star in each synthetic universe.

Table 1. Adopted Astrophysical Parameters

Parameter	Value	Description
$\eta_\oplus$	SAG13 power law	Fraction of sunlike stars w/exo-Earth candidate
R_p	$[R_p > 0.8/\sqrt{a},\ 1.4]\ R_\oplus$	Exo-Earth candidate planet radius[a]
a	[0.95, 1.67] AU	Semi-major axis for solar twin
e	0	Eccentricity (circular orbits)
$\cos i$	$[-1, 1]$	Cosine of inclination (uniform distribution)
ω	$[0, 2\pi]$	Argument of pericenter (uniform distribution)
M	$[0, 2\pi]$	Mean anomaly (uniform distribution)
Φ	Lambertian	Phase function
A_G	0.2	Geometric albedo of rocky planets
A_G	0.5	Geometric albedo of gas planets
z	Lindler model[b]	Average V band surface brightness of zodiacal
x	$22\,\mathrm{mag\,asec}^{-2}$	V band surface brightness of 1 zodi of exozodiacal dust[c]
n	LBTI nominal distribution	Distribution of number of zodis for all stars

[a] R_p lower bound is $R_p > 0.8/\sqrt{a}$ in units of $R_\oplus$, where a is the HZ-normalized semi-major axis in AU.[7]
[b] Lindler zodiacal light model as a function of ecliptic latitude and longitude at observation time
[c] For solar twin. Varied with spectral type, as zodi definition fixes optical depth.

We used the ExoCat-1 catalog,[21] as stored in the `MissionStars` table of the NASA Exoplanet Archive hosted by the NASA Exoplanet Science Institute (https://exoplanetarchive.ipac.caltech.edu/docs/data.html). Missing photometric information for targets is optionally synthesized by interpolating over Eric Mamajek's Mean Dwarf Stellar Color and Effective Temperature Sequence.[22] ExoCat-1 is further modified in the case when the binary leakage model is being used with updated information from the Washington Double-Star catalog, maintained at the U.S. Naval Observatory.

A.2 Instrument Inputs

The instrument parameters are shown in Table 2.

ACKNOWLEDGMENTS

Monte Carlo simulations in this study were run with GNU parallel.[23] Graphics in Figures 1 and 2 were produced in part with third-party code.[24,25] This information is predecisional and is provided for planning and discussion purposes only. Part of this research was carried out at the Jet Propulsion Laboratory, California Institute of Technology, under a contract with the National Aeronautics and Space Administration (80NM0018D0004).

REFERENCES

[1] National Academies of Sciences, Engineering, and Medicine, [*Pathways to Discovery in Astronomy and Astrophysics for the 2020s*], The National Academies Press, Washington, DC (2021).

[2] Morgan, R., Savransky, D., Turmon, M., Genszler, G., Mamajek, E. E., Robinson, T. D., and Stapelfeldt, K., "An exploration of expected number of exoplanets for a 6m class direct imaging observatory," in [*Space Telescopes and Instrumentation 2022: Optical, Infrared, and Millimeter Wave*], Coyle, L. E., Matsuura, S., and Perrin, M. D., eds., **12180**, 1218020, International Society for Optics and Photonics, SPIE (2022).

[3] National Academies of Sciences, Engineering, and Medicine, [*Exoplanet Science Strategy*], The National Academies Press, Washington, DC (2018).

[4] Stark, C. C., Roberge, A., Mandell, A., and Robinson, T. D., "Maximizing the exoearth candidate yield from a future direct imaging mission," *The Astrophysical Journal* **795**(2), 122 (2014).

[5] Feng, Y. K., Robinson, T. D., Fortney, J. J., Lupu, R. E., Marley, M. S., Lewis, N. K., Macintosh, B., and Line, M. R., "Characterizing earth analogs in reflected light: Atmospheric retrieval studies for future space telescopes," *The Astronomical Journal* **155**, 200 (apr 2018).

Table 2. Instrument Parameters

Parameter	6m Coronagraph	6m Starshade
Primary Diameter (m)	6.0	6.0
Obscuration Factor	0	0
Integration Time Limit	60 days	60 days
Starlight Suppression Performance		
Raw contrast floor	1×10^{-10}	4×10^{-11}
Raw contrast stability	2×10^{-11}	1×10^{-12}
Post-processing factor	0.29	0.29
Systematic noise floor	26.5	26.5
Core throughput	0.52	0.7
Photometric Aperture	0.7 λ/D	0.7 λ/D
Inner Working Angle, $IWA_{0.5}$	2.4 λ/D	1.89 λ/D
Inner Working Angle, $IWA_{0.1}$	1.5 λ/D	1.3 λ/D
Outer Working Angle	48 λ/D	200 λ/D
Bandwidth	20%	67%
Non-coronagraph Throughput		
Imaging Channel	0.28	–
Visible Spectral Channel	0.15	0.28
NIR Spectral Channel	0.31	0.38
Visible Detectors		
Quantum Efficiency	0.9	0.9
Photon Counting Efficiency	0.75	0.75
Dark Current (e/s)	3×10^{-5}	3×10^{-5}
Read Noise (e/pix)	0	0
Clock-Induced Charge (e/s)	1.3×10^{-5}	1.3×10^{-5}
NIR Detectors		
Quantum Efficiency	0.68	0.68
Dark Current (e/s)	1×10^{-5}	3×10^{-3}
Read Noise (e/pix)	0	0
Starshade		
Starshade Thrust (mN)	–	1800
Starshade Slew I_{sp} (s)	–	2900
Starshade Stationkeeping I_{sp} (s)	–	310
Starshade Wet Mass (kg)	–	15600
Starshade Dry Mass (kg)	–	5600
Starshade Separation (km)	–	92.5×10^{3}

[6] Gaudi, B. S., Seager, S., Mennesson, B., Kiessling, A., Warfield, K., Cahoy, K., Clarke, J. T., Domagal-Goldman, S., Feinberg, L., Guyon, O., Kasdin, J., Mawet, D., Plavchan, P., Robinson, T., Rogers, L., Scowen, P., Somerville, R., Stapelfeldt, K., Stark, C., Stern, D., Turnbull, M., Amini, R., Kuan, G., Martin, S., Morgan, R., Redding, D., Stahl, H. P., Webb, R., Alvarez-Salazar, O., Arnold, W. L., Arya, M., Balasubramanian, B., Baysinger, M., Bell, R., Below, C., Benson, J., Blais, L., Booth, J., Bourgeois, R., Bradford, C., Brewer, A., Brooks, T., Cady, E., Caldwell, M., Calvet, R., Carr, S., Chan, D., Cormarkovic, V., Coste, K., Cox, C., Danner, R., Davis, J., Dewell, L., Dorsett, L., Dunn, D., East, M., Effinger, M., Eng, R., Freebury, G., Garcia, J., Gaskin, J., Greene, S., Hennessy, J., Hilgemann, E., Hood, B., Holota, W., Howe, S., Huang, P., Hull, T., Hunt, R., Hurd, K., Johnson, S., Kissil, A., Knight, B., Kolenz, D., Kraus, O., Krist, J., Li, M., Lisman, D., Mandic, M., Mann, J., Marchen, L., Marrese-Reading, C., McCready, J., McGown, J., Missun, J., Miyaguchi, A., Moore, B., Nemati, B., Nikzad, S., Nissen, J., Novicki, M., Perrine, T., Pineda, C., Polanco, O., Putnam, D., Qureshi, A., Richards, M., Eldorado Riggs, A. J., Rodgers, M., Rud, M., Saini, N., Scalisi, D., Scharf, D., Schulz, K., Serabyn, G., Sigrist, N., Sikkia, G., Singleton, A., Shaklan, S., Smith, S., Southerd, B., Stahl, M., Steeves, J., Sturges, B., Sullivan, C., Tang, H., Taras, N., Tesch, J., Therrell, M., Tseng, H., Valente, M., Van Buren, D., Villalvazo, J., Warwick, S., Webb, D., Westerhoff, T., Wofford, R., Wu, G., Woo, J., Wood, M., Ziemer, J., Arney, G., Anderson, J., Maíz-Apellániz, J., Bartlett, J., Belikov, R., Bendek, E., Cenko, B., Douglas, E., Dulz, S., Evans, C., Faramaz, V., Feng, Y. K., Ferguson, H., Follette, K., Ford, S., García, M., Geha, M., Gelino, D., Götberg, Y., Hildebrand t, S., Hu, R., Jahnke, K., Kennedy, G., Kreidberg, L., Isella, A., Lopez, E., Marchis, F., Macri, L., Marley, M., Matzko, W., Mazoyer, J., McCandliss, S., Meshkat, T., Mordasini, C., Morris, P., Nielsen, E., Newman, P., Petigura, E., Postman, M., Reines, A., Roberge, A., Roederer, I., Ruane, G., Schwieterman, E., Sirbu, D., Spalding, C., Teplitz, H., Tumlinson, J., Turner, N., Werk, J., Wofford, A., Wyatt, M., Young, A., and Zellem, R., "The Habitable Exoplanet Observatory (HabEx) Mission Concept Study Final Report," *arXiv e-prints* , arXiv:2001.06683 (Jan. 2020).

[7] The LUVOIR Team, "The LUVOIR Mission Concept Study Final Report," *arXiv e-prints* , arXiv:1912.06219 (Dec. 2019).

[8] Damiano, M. and Hu, R., "Reflected spectroscopy of small exoplanets i: determining the atmospheric composition of sub-neptunes planets," *The Astronomical Journal* **162**(5), 200 (2021).

[9] Damiano, M. and Hu, R., "Reflected spectroscopy of small exoplanets ii: characterization of terrestrial exoplanets," *The Astronomical Journal* **163**(6), 299 (2022).

[10] Morgan, R., Savransky, D., Stark, C., and Nielsen, E., "The standard definitions and evaluation team final report: A common comparison of exoplanet yield." https://exoplanets.nasa.gov/system/internal_resources/details/original/1434_Standards_Team_Final_Report_20191007.pdf (2019).

[11] Shaklan, S., McKeithen, D. M., and Lisman, D., "A starshade for NASA's Habitable Worlds Observatory: exoplanet characterization from the UV to the NIR," in [*Techniques and Instrumentation for Detection of Exoplanets XI*], **12680**, 1268017, International Society for Optics and Photonics, SPIE (2023).

[12] Horning, A., Morgan, R., and Nielsen, E., "Minimum number of observations for exoplanet orbit determination," in [*Techniques and Instrumentation for Detection of Exoplanets IX*], *Proc. SPIE* **11117**, International Society for Optics and Photonics (2019).

[13] Morgan, R. M., Savransky, D., Turmon, M. J., Mennesson, B., Dula, W., Keithly, D. R., Mamajek, E. E., Newman, P., Plavchan, P., Robinson, T. D., Roudier, G., and Stark, C. C., "Faster Exo-Earth yield for HabEx and LUVOIR via extreme precision radial velocity prior knowledge," *Journal of Astronomical Telescopes, Instruments, and Systems* **7**(2), 021220 (2021).

[14] Plavchan, P., Vasisht, G., Beichman, C., Cegla, H., Dumusque, X., Wang, S., Gao, P., Dressing, C., and et al., "Earthfinder probe mission concept study: Characterizing nearby stellar exoplanet systems with earth-mass analogs for future direct imaging," *arXiv e-prints* , arXiv:2006.13428v1 (June 2020).

[15] Savransky, D. and the EXOSIMS team, "Exoplanet open-source imaging mission simulator." https://github.com/dsavransky/EXOSIMS (2020).

[16] Dulz, S., Plavchan, P., Crepp, J. R., Stark, C., Morgan, R., Kane, S., Newman, P., Matzko, W., and Mulders, G., "Joint Radial Velocity and Direct Imaging Planet Yield Calculations: I. Self-consistent Planet Populations," *The Astrophysical Journal* **893**(2) (2020).

[17] Kopparapu, R. K., Ramirez, R., Kasting, J. F., Eymet, V., Robinson, T. D., Mahadevan, S., Terrien, R. C., Domagal-Goldman, S., Meadows, V., and Deshpande, R., "Habitable Zones around Main-sequence Stars: New Estimates," *The Astrophysical Journal* **765**, 131 (3 2013).

[18] Sirbu, D., Belikov, R., Bendek, E., Henze, C., and Pluzhnik, E., "Demonstration of multi-star wavefront control for WFIRST, Habex, and LUVOIR," in [*Techniques and Instrumentation for Detection of Exoplanets IX*], Shaklan, S. B., ed., **11117**, 404 – 417, International Society for Optics and Photonics, SPIE (2019).

[19] Leinert, C., Bowyer, S., Haikala, L., Hanner, M., Hauser, M., Levasseur-Regourd, A., Mann, I., Mattila, K., Reach, W., Schlosser, W., et al., "The 1997 reference of diffuse night sky brightness," *Astronomy and Astrophysics Supplement Series* **127**(1), 1–99 (1998).

[20] Ertal2018Report, "Report on hosts survey return." http://nexsci.caltech.edu/missions/LBTI/report_hosts_dec2018_v1.2.pdf (2018).

[21] Turnbull, M. C., "Exocat-1: The nearby stellar systems catalog for exoplanet imaging missions." arXiv preprint arXiv:1510.01731 (2015).

[22] Mamajek, E., "A modern mean dwarf stellar color and effective temperature sequence." http://www.pas.rochester.edu/~emamajek/EEM_dwarf_UBVIJHK_colors_Teff.txt (2019).

[23] Tange, O., "Gnu parallel 20200522 ('kraftwerk')." https://doi.org/10.5281/zenodo.3841377 (May 2020).

[24] Charles, "(2020). cbrewer : colorbrewer schemes for matlab." https://www.mathworks.com/matlabcentral/fileexchange/34087-cbrewer-colorbrewer-schemes-for-matlab (2020).

[25] Kearney, K., "boundedline.m." https://github.com/kakearney/boundedline-pkg (2020).